

Piezoelectrically actuated silicon-nitride-based high-speed spatial light modulator

Received: 12 November 2024

Accepted: 7 November 2025

Published online: 26 November 2025

Check for updates

Tom Vanackere ^{1,2,8}✉, Artur Hermans ^{1,2,8}✉, Ian Christen ¹, Christopher Panuski ¹, Mark Dong ^{1,3}, Matthew Zimmermann ³, Hamza Raniwala¹, Andrew J. Leenheer ⁴, Matt Eichenfield^{4,5,6}, Gerald Gilbert ⁷ & Dirk Englund ¹✉

Advancements in light modulator technology have been driving discoveries and progress across various fields. The problem of large-scale coherent optical control of atomic quantum systems—including cold atoms, ions, and solid-state color centers—presents among the most stringent requirements. This motivates a new generation of high-speed large-scale modulator technology operating in the visible to near-infrared wavelength range. We introduce a scalable modulator technology based on piezoelectrically actuated silicon nitride resonant waveguide gratings fabricated on 200 mm diameter silicon wafers with CMOS-compatible processes. We present a proof-of-concept device with 4×4 individually addressable $50 \mu\text{m} \times 50 \mu\text{m}$ pixels or channels, each containing a resonant waveguide grating with a ~ 780 nm design wavelength, supporting > 100 MHz modulation speeds, and a spectral response with > 20 dB extinction.

Devices that have the ability to control multiple optical modes at high speeds are revolutionizing many fields of science and technology, including laser ranging¹, quantum information processing², imaging^{3,4}, optogenetics⁵, artificial intelligence^{6,7}, and augmented and virtual reality (AR/VR)^{8,9}. In particular, the availability of multimodal and/or high-speed light modulators has been instrumental in the rapid advancement of atom-based quantum technology over the last years^{2,10–13}. Optical control of atomic quantum systems poses the following requirements: (R1) operation at a design wavelength of choice in the visible (VIS) to near-infrared (NIR) spectrum, (R2) a scalable technology with a high channel density ($>100 \text{mm}^{-2}$), (R3) a high modulation speed (>100 MHz), and (R4) a high extinction ratio (>20 dB). This motivates the development of a new modulator technology, meeting these requirements to continue driving progress. Requirement (R1) stems from the fact that many optical transitions in atoms or atom-like emitters in solids lie in the visible (VIS) to near-infrared (NIR) wavelength range. VIS to NIR wavelength operation is also essential for bioimaging^{14,15}, optogenetics⁵, and AR/VR⁸. Requirement (R2), a scalable technology with a high channel density,

originates from the need to individually control hundreds to thousands of atoms to unlock quantum technology's full potential. High modulation speeds (R3) and high extinction ratios (R4) are required to optically control the state of atoms or atom-like emitters with high fidelity in a short time compared to the lifetime of the state¹³. A high-extinction and high-channel-density optical control technology acting as an ultrafast spatial light modulator is also an immediate benefit to the varied fields of research which already rely on devices with thousands to millions of times slower modulation rates.

Table 1 compares state-of-the-art multichannel light modulator technologies in terms of requirements (R1)–(R4). None of the existing technologies meets all requirements. Spatial light modulators (SLMs) operating in the VIS to NIR range based on microelectromechanical systems (MEMS)^{16–18} and liquid crystals^{19,20} are commercially available, but their modulation rates are limited. In the IR wavelength range, alternative SLM technologies with > 1 MHz modulation rates have been explored based on electrical gating of graphene^{21,22}, the Pockels effect in organic electro-optic molecules^{23–25} and dielectric thin films²⁶, the quantum-confined Stark effect in III-V semiconductor quantum-

¹Massachusetts Institute of Technology, Cambridge, MA, USA. ²Ghent University - imec, Ghent, Belgium. ³The MITRE Corporation, Bedford, MA, USA. ⁴Sandia National Laboratories, Albuquerque, NM, USA. ⁵University of Arizona, Tucson, AZ, USA. ⁶University of Colorado, Boulder, CO, USA. ⁷The MITRE Corporation, Princeton, NJ, USA. ⁸These authors contributed equally: Tom Vanackere, Artur Hermans. ✉e-mail: tomvac96@mit.edu; arturh@mit.edu; englund@mit.edu

well-based material^{27,28}, and charge carrier effects in indium tin oxide (ITO)²⁹ and silicon^{30,31}. The refractive index changes associated with these fast effects tend to be small, thus long interaction lengths are needed to realize devices with a high modulation efficiency. To create compact, free-space-coupled devices, one therefore often relies on optically resonant structures, such as metasurfaces^{21,22,24,28,29}, Fabry-Perot cavities²⁷, resonant waveguide gratings^{23,25,30}, or photonic crystal cavities³¹.

To fulfill requirements (R1)–(R4), we introduce an SLM technology based on piezoelectrically actuated silicon nitride (SiN) resonant waveguide gratings (Fig. 1). The piezoelectric actuators induce strain in the gratings, resulting in a shift of the resonant wavelengths and thereby realizing free-space-coupled modulators. This technology not only enables SLMs with $\mathcal{O}(MHz)$ to $\mathcal{O}(GHz)$ modulation rates, it also operates in the VIS to NIR wavelength range. Moreover, our devices are fabricated on 200 mm diameter silicon wafers using deep ultraviolet (UV) optical lithography and CMOS-compatible (complementary-metal-oxide-semiconductor-compatible), low-temperature processes (see Methods for fabrication details). Hence, we can fabricate the piezoelectric actuators and resonant waveguide gratings directly on top of electronics to drive the devices³² or on (multiple) metal layers to enable large-scale electrical interconnects. These integration schemes are advantageous for the commercial production of large-scale SLMs.

Table 1 | Comparison of multichannel light modulator technologies in terms of requirements (R1)–(R4)

Technology	R1	R2	R3	R4
Liquid-Crystal-on-Silicon (LCoS) ^{19,20}	✓	✓	✗	✓
Digital Micromirror Device (DMD) ^{9,16}	✓	✓	✗	✓
Grating Light Valve (GLV) ^{9,17}	✓	✓	✗	✓
Atom-control Photonic Integrated Circuit (APIC) ^{b,13}	✓	✗	✓	✓
Electro-optic silicon-organic metasurface ²⁵	✗	✗	✓	✗
Silicon photonic crystal cavities with free-carrier modulation ³¹	✗	✓	✓	-
Technology presented in this work	✓	✓	✓	✓

^aMEMS device.

^bSiN PIC with AlN piezoelectric actuators.

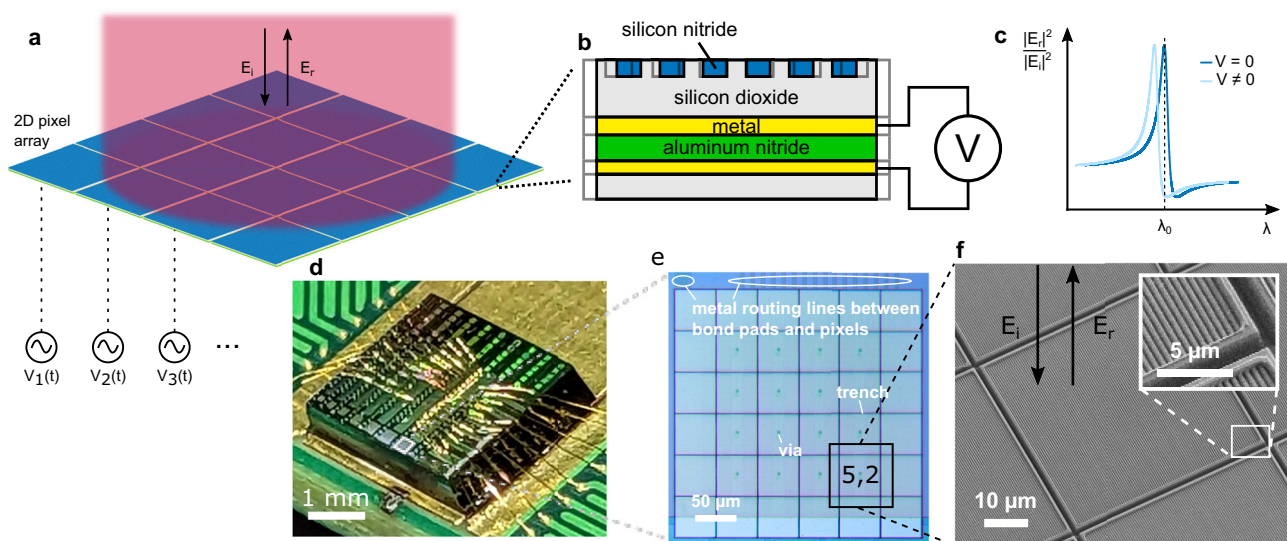


Fig. 1 | Concept and device images. **a, b** Concept figure of our spatial light modulator (SLM) technology based on piezoelectrically actuated SiN resonant waveguide gratings. The piezoelectric actuators are based on AlN thin films. **c** Device operation principle. Applying a voltage shifts the reflection spectrum. **d** Chip with

Our work builds on a platform developed at Sandia National Laboratories consisting of a SiN optical waveguide layer on top of an aluminum-nitride-based (AlN) piezoelectric actuation layer³³. While previous works on this platform focused on photonic integrated circuits^{13,33–35}, here we demonstrate densely packed free-space-coupled modulators arranged in a 4×4 grid with a high fill factor of $\sim 96\%$ as a proof of concept for scalable SLM technology (Fig. 1). To boost the modulation efficiency of our devices we not only make use of optically resonant devices, namely resonant waveguide gratings³⁶, but we also take advantage of the mechanical resonances of our pixels, which greatly enhances the piezoelectrically induced displacement³⁷. Resonant waveguide gratings, also known as guided mode resonant gratings or waveguide-mode resonant gratings, couple light incident at specific wavelengths, incidence angles, and polarization to leaky guided modes, giving rise to resonances in the reflection and transmission spectra (in amplitude and phase)³⁶.

Results

Design

We designed our SiN resonant waveguide gratings to operate at a wavelength λ of ~ 780 nm (R1), with a pitch Λ of $0.490 \mu\text{m}$ for a SiN thickness of $0.3 \mu\text{m}$. The simulated reflection spectrum of our gratings,

$R[dB] = 10 \times \log_{10} \left(\frac{|E_{out}(\lambda)|^2}{|E_{ref}(\lambda)|^2} \right)$, in Fig. 2a shows a steep dip at a wavelength

of ~ 800 nm with an extinction ratio > 50 dB (R4) with respect to the reflection at ~ 770 nm. We test our devices in a cross-polarized light setup, as schematically depicted below (see Supplementary Fig. 1 for more details). Our simulation of the reflection spectrum captures the cross-polarized testing method (see Methods for more information). The steep dip in the reflection spectrum results from the phase difference between TE and TM polarized reflected light shifting from 0 to π while the reflection amplitude of TE and TM fields remain similar (Fig. 2c), where TE polarized light corresponds to the electric field being parallel to the grating lines. When the TE and TM polarized light waves reflected off the grating are in phase with equal amplitude, the reflected light is polarized at 0° before the polarizing beamsplitter and no light is reflected towards the detector. For a phase difference of π all light is reflected. Notably, the effective interferometer governing this effect is contained within $\sim 1 \mu\text{m}$ of thickness of the device, requiring no long-pathlength stabilization.

4×4 SLM wire bonded to a printed circuit board (PCB). See Methods for packaging details. **e** Microscope image of 4×4 SLM with a $50 \mu\text{m}$ pixel pitch and $1 \mu\text{m}$ wide trenches in between pixels. **f** Scanning electron microscope (SEM) image showing a grating surrounded by trenches.

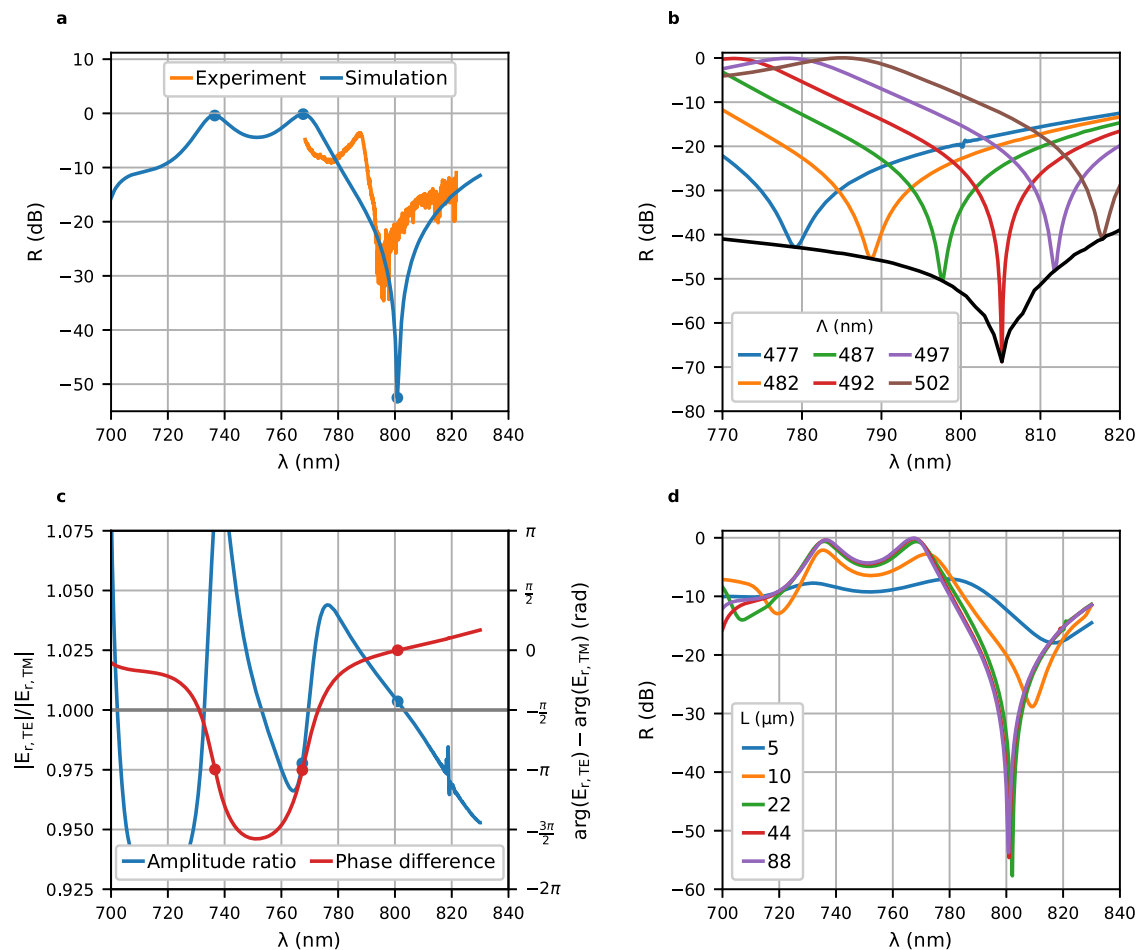


Fig. 2 | Device design, optical. **a** Simulated reflection spectrum compared to the measured spectrum, with $R[\text{dB}] = 10 \times \log_{10} \left(\frac{|E_{\text{out}}(\lambda)|^2}{|E_{\text{ref}}(\lambda)|^2} \right)$. **b** Influence of the grating pitch Λ on the reflection spectrum. These simulations are all for a duty cycle of 63%. **c** The simulated amplitude ratio and phase difference between TE and TM polarized reflected waves. The dots indicate the wavelengths at which there is a 0 and $-\pi$

phase difference, corresponding to the minima and maxima in (a). **d** Simulation of reflection spectrum for different grating sizes L . For a fair comparison the Gaussian input beam was rescaled such that the $1/e$ field full width is kept at 45% of the grating size. This way, equal proportions of the input beam interact with the grating structure for all pixel sizes.

A decrease in grating pitch blue-shifts the wavelength of the dip in the reflection spectrum (Fig. 2b). A pitch of 492 nm gives a maximum extinction ratio of >60 dB. The reduced extinction ratio at different pitches results from the ratio between the TE and TM reflection amplitudes being further away from 1 where the phase difference is 0.

By reducing the grating pitch to $0.27 \mu\text{m}$, we can shift the optical resonance all the way down to ~ 470 nm, the short wavelength end of the visible spectrum (see Supplementary Fig. 3). Our technology can operate at a design wavelength of choice in the VIS to near-IR spectrum simply by altering the pitch of the grating (R1).

Our simulations take into account the finite size of the gratings and the incident light beam. While the fabricated and tested devices have a grating size L of $49 \mu\text{m}$ (Fig. 1e), simulations indicate that we could reduce the size down to $\sim 20 \mu\text{m}$ without significant changes in extinction ratio and the overall shape of the reflection spectrum (Fig. 2d), resulting in even higher channel densities (R2).

The material platform with which we are working allows fabrication of undercut devices (see Methods), giving us an additional degree of freedom in engineering the mechanical device properties. We can produce pixels of length L supported by a pillar of size l underneath (schematically shown in Fig. 3a, SEM image in Fig. 3b), where L and l can be chosen freely for every pixel. The pillar also contains electrical vias between the piezoelectric actuator and a bottom metal routing layer, connecting the pixels to bond pads (see Fig. 1d, e). Figure 3c

shows the simulated mechanical mode with an eigenfrequency f_r of 5.9 MHz for a device with $L = 49 \mu\text{m}$ and $l = 10 \mu\text{m}$. This closely matches the resonance observed experimentally, Fig. 4b, c. By altering the pixel and pillar size L and l , we can set the mechanical resonance to a frequency of choice (Fig. 3d).

Characterization

Figures 4a and 2a show the measured reflection spectrum of a grating and its agreement with simulations, with a measured extinction ratio > 20 dB (R4). We measure the modulation amplitude A and speed of the packaged devices by reflecting laser light off a pixel and detecting the reflected light (with electric field E_{out}) on a fast photodiode (Fig. 4e), which is connected to an electrical spectrum analyzer (ESA). When applying an AC voltage to the illuminated pixel, a peak appears on the ESA at the applied AC frequency f , as anticipated for our piezoelectrically actuated device. The height of this peak, i.e. the modulation amplitude A , depends on the laser wavelength. Figure 4a overlaps the reflection spectrum with the modulation amplitude as a function of wavelength λ . The peak of the modulation amplitude occurs where the slope in the reflection spectrum is steepest (~ 791 nm). The devices have an optical bandwidth of several nanometers (8 nm peak to trough of resonance, 3 dB bandwidth of 2.3 nm in the modulation amplitude measurement). This corresponds to photon-lifetime-limited modulation bandwidths on the order of 1 THz,

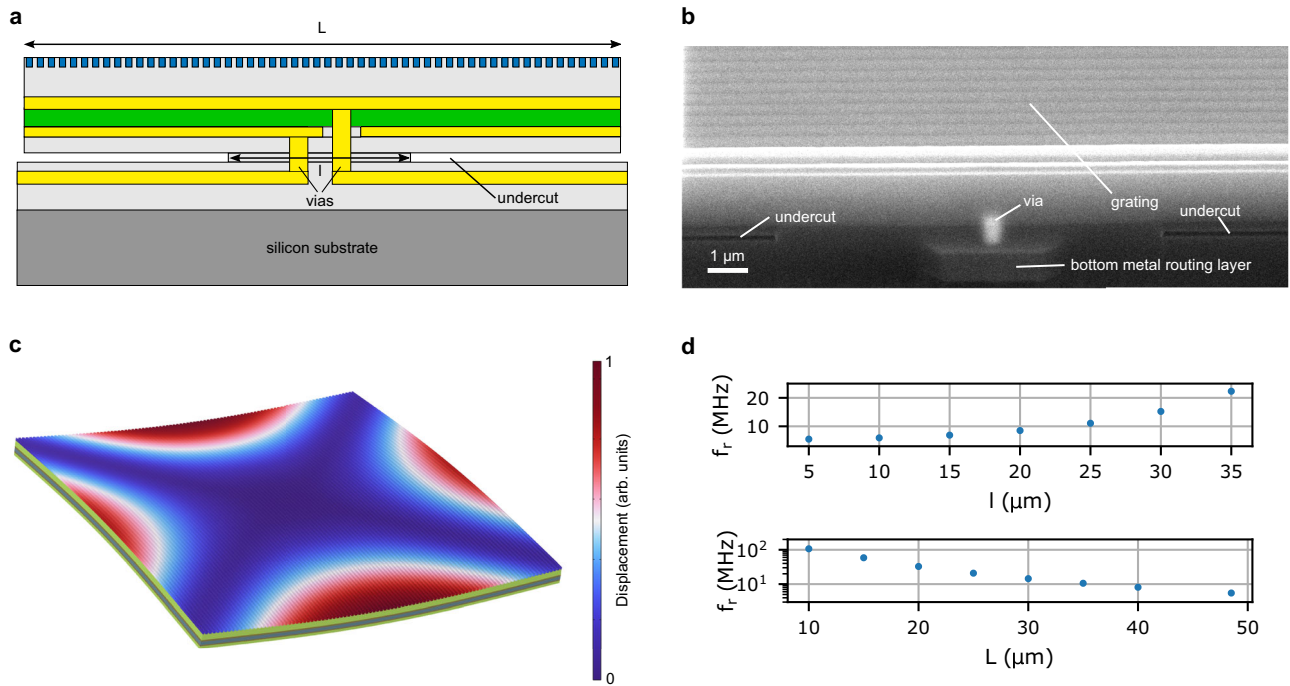


Fig. 3 | Device design, mechanical. **a** Schematic cross-section of a released device with grating size L . Released devices are undercut and anchored to the substrate with a silicon dioxide pillar, with diameter l , in the middle of the grating. **b** SEM image of a cross-section of a released device (at an angle of 57.5°). We used focused ion beam milling (FIB) to create a hole in the device so we could image the cross-

section. This is an image of the middle of a grating, where it is anchored to the substrate. **c** Simulated mechanical mode with an eigenfrequency f_r of 5.9 MHz for a released device with $L = 49 \mu\text{m}$ and $l = 10 \mu\text{m}$. Simulated in COMSOL. **d** Simulated eigenfrequency f_r as a function of pillar diameter l for grating size $L = 49 \mu\text{m}$ (top) and simulated f_r as a function of L for $l = 5 \mu\text{m}$ (bottom).

which does not pose a limitation for the envisaged applications. Moreover, the target applications typically only require modulators with narrowband operation at a discrete set of wavelengths (e.g. a set of wavelengths corresponding to certain atomic transitions). Our modulator technology is very well suited to accommodate this requirement. Either one can use separate modulator chips designed to operate at different wavelengths, or pixels designed to operate at different wavelengths can be integrated on the same chip (in separate chip areas or interleaved).

Figure 4b compares the modulation amplitude and speed for two different types of devices, released and unreleased. Released devices are undercut and anchored to the substrate with a $10 \mu\text{m}$ wide silicon dioxide pillar in the middle of the pixel (see Methods for fabrication details and Fig. 3b for an SEM image of a device cross-section). Unreleased devices have no undercut. The goal of releasing is to make the devices more mechanically compliant, resulting in lower drive voltages for the same level of induced strain. Additionally, released devices have high-quality-factor mechanical resonances. Resonant enhancement reduces the required drive voltage even further. Figure 4b shows the wavelength shift $\Delta\lambda_r/\Delta V$ of the reflection spectrum versus the applied AC frequency f for a released and unreleased grating. We calculate the wavelength shift from the measured modulation amplitude and the slope of the reflection spectrum. The numerous peaks and troughs in Fig. 4b are attributed to mechanical resonances^{38,39}. The more compliant nature of the released devices results in low-frequency wavelength shifts that are more than an order of magnitude larger compared to the unreleased devices. It also leads to the appearance of mechanical resonances at lower frequencies. Finite element analysis confirms the existence of mechanical resonances and identifies the mechanical mode at $f_r \approx 5 \text{ MHz}$ for the released device (Fig. 3c). The resonance at $f_r \approx 5 \text{ MHz}$ gives a large wavelength shift of $4 \times 10^2 \text{ pm V}^{-1}$, which corresponds to an enhancement of a factor $k = \frac{(\Delta\lambda_r/\Delta V)_{f_r}}{(\Delta\lambda_r/\Delta V)_{DC}} \approx 50$ compared to the low-frequency shift. Up to a frequency of $\sim 100 \text{ MHz}$, the data shows wavelength shifts larger than the low-frequency

response for the released device (R3). The stiffer nature of the unreleased device shifts the resonances to higher frequencies. Up to $\sim 700 \text{ MHz}$, wavelength shifts are comparable to the low-frequency response. The frequency response measurements are limited by the photodetector bandwidths (DC-400 MHz for the released device and 5–1000 MHz for the unreleased device measurement) and the 900 MHz bandwidth of the voltage amplifiers on the printed circuit boards (see Methods).

From the frequency response measurements (Fig. 4b) and the measured reflection spectrum (Fig. 4a), we can estimate the voltages required to shift the spectrum by 8 nm, that is, the wavelength difference between the trough and peak in the spectrum. We find a voltage of $\sim 20 \text{ V}$ for a released device at the $\sim 5 \text{ MHz}$ mechanical resonance and $\sim 1 \times 10^3 \text{ V}$ off-resonance (100 kHz driving frequency). For an unreleased device, we estimate a voltage of $\sim 40 \times 10^3 \text{ V}$ off-resonance (at 10 MHz). We recognize that the off-resonance and unreleased device voltages are high in this proof-of-concept demonstration and suggest ways of lowering these significantly in the discussion. Also, we note that several technologies exist today to deliver voltages in the $\mathcal{O}(10 \text{ V})$ to $\mathcal{O}(k\text{V})$ range at $\mathcal{O}(\text{MHz})$ to $\mathcal{O}(\text{GHz})$ frequencies, such as Si LDMOS (laterally-diffused metal-oxide semiconductor)⁴⁰, SiC⁴¹, and GaN-based devices⁴².

Figure 4d shows the ringdown measurement of the mechanical mode at $\sim 5 \text{ MHz}$ for a released device. Fitting the data gives a ring-down time τ of $3.1 \mu\text{s}$. This corresponds to a mechanical Q -factor of $Q_m = \frac{\omega_m \tau}{2} = 52$ ($\omega_m = 2\pi \times 5.3 \text{ MHz}$)⁴³. This is in good agreement with the enhancement factor of ~ 50 observed in the frequency response measurement, as expected for a harmonic oscillator.

Pixel-to-pixel fabrication-induced variations lead to differences in resonance frequencies and enhancement factors, e.g. variations in pixel size, layer thicknesses, and depth of the undercut. For the pixels in our 4×4 device, we determined the mechanical resonance frequencies f_r of the strong resonance around 5 MHz and the associated enhancement factor k (Fig. 4c). The average resonance frequency is

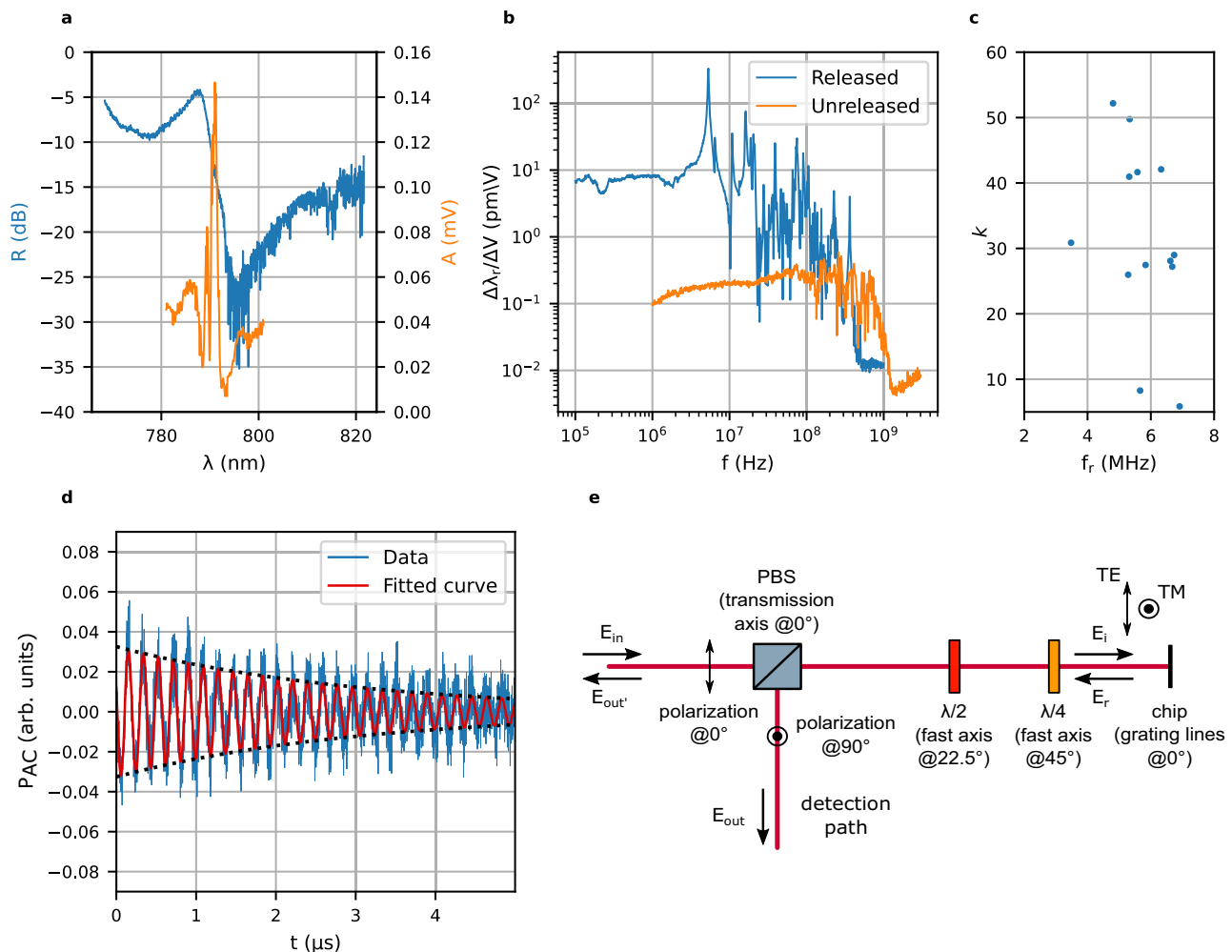


Fig. 4 | Device characterization. **a** The reflection spectrum of the grating (blue) overlapped with the modulation amplitude A as a function of wavelength (orange), measured on an unreleased device at a fixed AC frequency f of 20 MHz for a peak-to-peak voltage of 10 V. **b** Wavelength shift $\Delta\lambda_r/\Delta V$ versus AC frequency f for a released and unreleased device. We used a detector with a 3 dB bandwidth of DC-400 MHz for the released device and 5–1000 MHz for the unreleased device. **c** Measurement of the different mechanical resonance frequencies f_r for each pixel of the strong resonance around 5 MHz and the associated enhancement factor k . 13

of the 16 pixels were functioning in this device. All measurements were done at a wavelength of 791 nm. **d** Ringdown measurement of the mechanical mode at ~ 5 MHz of a released device. For this measurement we first apply an AC frequency at resonance, then we switch it off and observe how the AC-coupled photodiode signal P_{AC} decays over time t on an oscilloscope. Fitting gives a ringdown time τ of 3.1 μ s. **e** Schematic depiction of our cross-polarized light setup. PBS: polarizing beamsplitter, $\lambda/2$: half-wave plate, $\lambda/4$: quarter-wave plate.

5.7 MHz (standard deviation of 0.9 MHz) and the average enhancement factor is 32 (standard deviation of 13). Established post-fabrication trimming techniques such as laser trimming⁴⁴ and focused ion beam (FIB) milling⁴⁵ can be used to tune up the resonances. A possible approach for closed-loop laser trimming consists of combining the trimming laser, probe laser (to be modulated by the device), and imaging optics in a single optical system, as has been demonstrated for photonic crystal cavities³¹ and ring resonators¹³. Image recognition methods can locate the pixel edges to be trimmed⁴⁴. We can parallelize laser trimming of multiple pixels by e.g. using a liquid crystal SLM to generate arrays of laser spots and photodetector arrays for probe laser detection.

Discussion

One of the main challenges ahead is to reduce the voltages required to achieve high-extinction-ratio modulation. We see several ways to achieve this. Firstly, we can use a piezoelectric material with an enhanced response. Scandium aluminum nitride, for instance, has a piezoelectric response up to 5 times larger compared to AlN⁴⁶. Secondly, we can use optical resonators with reduced optical linewidths.

Recently, a silicon-nitride-based resonant waveguide grating with a linewidth of only ~ 0.7 μ m at 779 nm has been demonstrated⁴⁷. Vertically coupled photonic crystal cavities with high quality factors are another promising candidate. These have been demonstrated in silicon with linewidths < 10 μ m at a wavelength of 1.6 μ m³¹. Silicon nitride photonic crystal cavities with linewidths down to 0.1 μ m at 760 nm have been reported⁴⁸, though these were not vertically coupled. By combining narrow-linewidth optical resonators with piezoelectric materials with an enhanced response, we can potentially reduce the drive voltages by three to four orders of magnitude. A significant reduction in linewidth will increase the need for post-fabrication optical resonance tuning, as the resonant wavelength is likely to deviate from the target operating wavelength. This is a common problem in integrated optics for which multiple solutions have been reported, e.g. laser trimming^{13,31} and on-chip heaters^{13,49}.

Another challenge is to get all the required electrical driving signals onto the SLM chip as we scale up the number of pixels. In our proof-of-concept device we use wire bonds. The number of wire bonds is limited by the available chip perimeter. For example, on a 1 cm by 1 cm chip, for a pixel size of 50 μ m and a typical bond pad spacing of

100 μm , we can fit 40,000 pixels, but only 400 bond pads around the chip perimeter. One approach to increase the number of electrical inputs is to make use of through-silicon vias⁵⁰ and bond the SLM chip to an interposer. This interposer could also hold electronic driving ICs. An even more advanced solution is to integrate some of the electronics on the SLM chip.

We see many potential applications for this SLM technology. Depending on the target application, we can configure our modulator technology in different ways. For instance, driving the modulators at a strong mechanical resonance generates strong sidebands to the incident laser light (the sidebands could be resonant with an atomic transition). The generation of these sidebands can be switched on and off (individually controlled for every pixel) with response times on the order of microseconds, with the exact response time depending on the mechanical quality factor. This has applications in the optical control of atomic systems, where one wishes to address certain atomic transitions in large-scale arrays of atoms, ions, or solid-state color centers¹³. We can use different mechanical resonances to generate sidebands at different frequencies or engineer the pixels to alter the mechanical resonances, e.g. by varying the grating size or the depth of the undercut. Laser trimming^{31,44} or focused ion beam milling⁴⁵ can alter the resonance frequencies post-fabrication.

Predictable time-varying and even periodically repeating light patterns can be generated in the far field³⁸ by driving each of the pixels at a particular mechanical resonance frequency, enabling low-voltage driving, with a particular phase. The generated pattern will depend on the chosen frequencies and phases. This concept has been described for photonic integrated circuit phased arrays³⁸ and has applications in atom control⁵¹, display technology⁵², and laser ranging⁵³. The proposed SLM technology enables MHz speeds, compared to conventional MEMS laser scanners limited to sub-MHz speeds⁵².

Our modulator technology could even generate arbitrary waveforms requiring the full device bandwidth (i.e. not only driving at resonance frequencies) by using signal equalization techniques to compensate for the non-flat frequency response. Signal equalization has been demonstrated for photonic integrated circuit modulators with mechanical resonances in the MHz to GHz range³⁹.

In conclusion, we have presented a scalable high-channel-density, high-speed modulator technology operating in the visible to near-infrared spectrum. This technology has the potential to drive progress across various fields in science and technology, including large-scale coherent optical control of atomic quantum systems.

Methods

Fabrication

Our devices consist of a silicon nitride (SiN) optical waveguide layer on top of an aluminum-nitride-based (AlN) piezoelectric actuation layer with a silicon dioxide optical buffer layer in between^{33–35}. The devices are fabricated on 200 mm diameter silicon wafers at Sandia National Laboratories using deep ultraviolet (UV) optical lithography. Low-temperature, CMOS-compatible processes are used for thin-film deposition, namely plasma-enhanced chemical vapor deposition (PECVD; for amorphous silicon, SiN and oxide deposition) and physical vapor deposition (PVD; for AlN and metal deposition). There are three metal layers in the stack to enable device actuation. From bottom to top, these are: a routing layer which we use to connect each of the pixels to bond pads, a bottom electrode layer, and a top electrode layer. In between the two electrode layers there is the AlN layer; together these comprise the piezoelectric actuation layer. The bottom electrode layer is separated from the routing layer by a silicon dioxide buffer. The three metal layers are connected by vias. Throughout the process flow, chemical-mechanical polishing (CMP) is used for planarization. In between the bottom electrode layer and routing layer there is also a patterned amorphous silicon layer to enable undercutting of devices. After having processed the entire device stack, a

release etch in XeF₂ gas removes the amorphous silicon to create undercut devices. The XeF₂ gas can reach the amorphous silicon layer through deep, etched trenches.

Packaging

We dice the wafers into chips and wire bond them to printed circuit boards (Fig. 1d). The devices with 4×4 pixels have 17 bond pads, 1 pad for a shared ground and 16 pads for the signals applied to each of the pixels. Each of our PCBs contains 16 operational amplifiers (OPAMPs; Texas Instruments THS3491) to individually address 16 pixels. The OPAMPs provide a voltage gain of 5, have a 900 MHz bandwidth, and a ± 16 V supply voltage. Ganged microscale RF plugs (Samtec) connect the PCBs to signal generators.

Simulation

We use Ansys Lumerical's 2D FDTD solver for optical simulations. We run the simulation for two orthogonal polarizations. Afterwards, we use transfer matrix multiplication to implement the beamsplitter and wave plates together with the simulations of both polarizations. Our simulation takes into account the Gaussian shape of the excitation and collected beams. To directly compare the simulation with the measurement, we implement the same normalization method. We perform a simulation without the grating structure to simulate the effect of reflection from the aluminum layer with the silicon dioxide and SiN layers on top (E_{ref}). The resulting simulation is able to capture the entire measurement setup to accurately predict the results.

Data availability

The data generated in this study have been deposited in the Zenodo database under accession code <https://doi.org/10.5281/zenodo.17265890>.

References

- Park, J. et al. All-solid-state spatial light modulator with independent phase and amplitude control for three-dimensional LiDAR applications. *Nat. Nanotechnol.* **16**, 69–76 (2021).
- Ebadi, S. et al. Quantum phases of matter on a 256-atom programmable quantum simulator. *Nature* **595**, 227–232 (2021).
- Nikolenko, V. et al. SLM microscopy: scanless two-photon imaging and photostimulation using spatial light modulators. *Front. Neural Circ.* **2**, 5 (2008).
- Yoon, S. et al. Deep optical imaging within complex scattering media. *Nat. Rev. Phys.* **2**, 141–158 (2020).
- Ronzitti, E. et al. Recent advances in patterned photostimulation for optogenetics. *J. Opt.* **19**, 113001 (2017).
- Zuo, Y., Zhao, Y., Chen, Y.-C., Du, S. & Liu, J. Scalability of all-optical neural networks based on spatial light modulators. *Phys. Rev. Appl.* **15**, 054034 (2021).
- Bernstein, L. et al. Single-shot optical neural network. *Sci. Adv.* **9**, eadg7904 (2023).
- Chang, C., Bang, K., Wetzstein, G., Lee, B. & Gao, L. Toward the next-generation VR/AR optics: a review of holographic near-eye displays from a human-centric perspective. *Optica* **7**, 1563–1578 (2020).
- Zhan, T., Yin, K., Xiong, J., He, Z. & Wu, S.-T. Augmented reality and virtual reality displays: perspectives and challenges. *iScience* **23**, 101397 (2020).
- Wright, K. et al. Benchmarking an 11-qubit quantum computer. *Nat. Commun.* **10**, 5464 (2019).
- Christen, I. et al. An integrated photonic engine for programmable atomic control. *Nat. Commun.* **16**, 82 (2025).
- Graham, T. M. et al. Multi-qubit entanglement and algorithms on a neutral-atom quantum computer. *Nature* **604**, 457–462 (2022).
- Menssen, A. J. et al. Scalable photonic integrated circuits for high-fidelity light control. *Optica* **10**, 1366–1372 (2023).

14. Lichtman, J. W. & Conchello, J.-A. Fluorescence microscopy. *Nat. Methods* **2**, 910–919 (2005).
15. Yoon, S. et al. Recent advances in optical imaging through deep tissue: imaging probes and techniques. *Biomater. Res.* **26**, 57 (2022).
16. Hornbeck, L. J. Digital Light Processing for high-brightness high-resolution applications. In *International Society for Optics and Photonics* (ed. Wu, M. H.) 27–40 (SPIE, 1997).
17. Bloom, D. M. Grating light valve: revolutionizing display technology. In *International Society for Optics and Photonics* (ed. Wu, M. H.) 165 – 171 (SPIE, 1997).
18. Tzang, O. et al. Wavefront shaping in complex media with a 350 kHz modulator via a 1D-to-2D transform. *Nat. Photonics* **13**, 788–793 (2019).
19. McKnight, D. J., Johnson, K. M. & Serati, R. A. 256 × 256 liquid-crystal-on-silicon spatial light modulator. *Appl. Opt.* **33**, 2775–2784 (1994).
20. Zhang, Z., You, Z. & Chu, D. Fundamentals of phase-only liquid crystal on silicon (LCOS) devices. *Light.: Sci. Appl.* **3**, e213 (2014).
21. Fan, K., Suen, J., Wu, X. & Padilla, W. J. Graphene metamaterial modulator for free-space thermal radiation. *Opt. Express* **24**, 25189–25201 (2016).
22. Zeng, B. et al. Hybrid graphene metasurfaces for high-speed mid-infrared light modulation and single-pixel imaging. *Light.: Sci. Appl.* **7**, 51 (2018).
23. Benea-Chelmus, I.-C. et al. Electro-optic spatial light modulator from an engineered organic layer. *Nat. Commun.* **12**, 5928 (2021).
24. Sun, X. et al. Electro-optic polymer and silicon nitride hybrid spatial light modulators based on a metasurface. *Opt. Express* **29**, 25543–25551 (2021).
25. Benea-Chelmus, I.-C. et al. Gigahertz free-space electro-optic modulators based on Mie resonances. *Nat. Commun.* **13**, 3170 (2022).
26. Smolyaninov, A., El Amili, A., Vallini, F., Pappert, S. & Fainman, Y. Programmable plasmonic phase modulation of free-space wavefronts at gigahertz rates. *Nat. Photonics* **13**, 431–435 (2019).
27. Worchesky, T. L., Ritter, K. J., Martin, R. & Lane, B. Large arrays of spatial light modulators hybridized to silicon integrated circuits. *Appl. Opt.* **35**, 1180–1186 (1996).
28. Lee, J. et al. Ultrafast electrically tunable polaritonic metasurfaces. *Adv. Opt. Mater.* **2**, 1057–1063 (2014).
29. Huang, Y.-W. et al. Gate-tunable conducting oxide metasurfaces. *Nano Lett.* **16**, 5319–5325 (2016).
30. Shuai, Y.-C. et al. Coupled bilayer photonic crystal slab electro-optic spatial light modulators. *IEEE Photonics J.* **9**, 7101411 (2017).
31. Panuski, C. L. et al. A full degree-of-freedom spatiotemporal light modulator. *Nat. Photonics* **16**, 834–842 (2022).
32. Lee, Y. H. D. & Lipson, M. Back-end deposited silicon photonics for monolithic integration on CMOS. *IEEE J. Sel. Top. Quant. Electron.* **19**, 8200207 (2013).
33. Stanfield, P. R., Leenheer, A. J., Michael, C. P., Sims, R. & Eichenfield, M. CMOS-compatible, piezo-optomechanically tunable photonics for visible wavelengths and cryogenic temperatures. *Opt. Express* **27**, 28588–28605 (2019).
34. Dong, M. et al. High-speed programmable photonic circuits in a cryogenically compatible, visible-near-infrared 200 mm CMOS architecture. *Nat. Photonics* **16**, 59–65 (2022).
35. Dong, M. et al. Piezo-optomechanical cantilever modulators for VLSI visible photonics. *APL Photonics* **7**, 051304 (2022).
36. Quaranta, G., Basset, G., Martin, O. J. F. & Gallinet, B. Recent advances in resonant waveguide gratings. *Laser Photonics Rev.* **12**, 1800017 (2018).
37. Li, B.-B., Ou, L., Lei, Y. & Liu, Y.-C. Cavity optomechanical sensing. *Nanophotonics* **10**, 2799–2832 (2021).
38. Dong, M. et al. Synchronous micromechanically resonant programmable photonic circuits. *Nat. Commun.* **14**, 7716 (2023).
39. Wen, Y. H. et al. Strain-concentration for fast, compact photonic modulation and non-volatile memory. *Optica* **11**, 1511–1518 (2024).
40. Johansson, T. & Fritzin, J. A review of watt-level CMOS RF power amplifiers. *IEEE Trans. Microw. Theory Tech.* **62**, 111–124 (2013).
41. Jørgensen, A. B., Aunsborg, T. S., Beczkowski, S., Uhrenfeldt, C. & Munk-Nielsen, S. High-frequency resonant operation of an integrated medium-voltage SiC MOSFET power module. *IET Power Electron.* **13**, 475–482 (2020).
42. Krause, S., Brückner, P., Dammann, M. & Quay, R. High-power-density AlGaIn/GaN technology for 100-V operation at L-band frequencies. In *2019 IEEE International Electron Devices Meeting (IEDM)*, 17.4.1–17.4.4 (IEEE, 2019).
43. Thompson, J. D. et al. Strong dispersive coupling of a high-finesse cavity to a micromechanical membrane. *Nature* **452**, 72–75 (2008).
44. Liu, Y., Zhao, Q., Zhang, D. & Cui, J. Automatic pico laser trimming system for silicon MEMS resonant devices based on image recognition. *IEEE Trans. Semiconduct. Manuf.* **36**, 260–267 (2023).
45. Efimovskaya, A., Wang, D. & Shkel, A. M. Mechanical trimming with focused ion beam for permanent tuning of MEMS dual-mass gyroscope. *Sens. Actuators A: Phys.* **313**, 112189 (2020).
46. Akiyama, M. et al. Enhancement of piezoelectric response in scandium aluminum nitride alloy thin films prepared by dual reactive cosputtering. *Adv. Mater.* **21**, 593–596 (2009).
47. Fang, J. et al. Million-Q free space meta-optical resonator at near-visible wavelengths. *Nat. Commun.* **15**, 10341 (2024).
48. Fryett, T. K. et al. Encapsulated silicon nitride nanobeam cavity for hybrid nanophotonics. *ACS Photonics* **5**, 2176–2181 (2018).
49. Campenhout, J. V., Green, W. M. J., Assefa, S. & Vlasov, Y. A. Integrated NiSi waveguide heaters for CMOS-compatible silicon thermo-optic devices. *Opt. Lett.* **35**, 1013–1015 (2010).
50. Wang, J. et al. A short review of through-silicon via (TSV) interconnects: Metrology and analysis. *Appl. Sci.* **13**, 8301 (2023).
51. Dong, M. et al. Programmable photonic integrated meshes for modular generation of optical entanglement links. *npj Quant. Inf.* **9**, 42 (2023).
52. Holmström, S. T. S., Baran, U. & Urey, H. MEMS laser scanners: A review. *J. Microelectromech. Syst.* **23**, 259–275 (2014).
53. Zhang, X., Kwon, K., Henriksson, J., Luo, J. & Wu, M. C. A large-scale microelectromechanical-systems-based silicon photonics LiDAR. *Nature* **603**, 253–258 (2022).

Acknowledgements

We acknowledge funding from MITRE’s Quantum Moonshot program, the Defense Advanced Research Projects Agency (ONISQ program), the NSF Center for Quantum Networks, and the Air Force Research Laboratory. This work is supported by a collaboration between the US DOE and other Agencies. This material is based upon work supported by the U.S. Department of Energy, Office of Science, National Quantum Information Science Research Centers, Quantum Systems Accelerator. T.V. and A.H. thank the Research Foundation - Flanders (FWO) for financial support (PhD fellowship 11F5322N and postdoctoral fellowship 1258423N). D.E. acknowledges partial support from Honda Research Institute USA, Inc., and from the NSF Eager program. C.P. was supported by the Hertz Foundation Elizabeth and Stephen Fantone Family Fellowship. M.E. performed this work, in part, at the Center for Integrated Nanotechnologies, an Office of Science User Facility operated for the U.S. Department of Energy (DOE) Office of Science. Simulations were supported in part by Army Research Office grant W911NF-20-1-0084 supervised by M. Gerhold. Sandia National Laboratories is a multimission laboratory managed and operated by National Technology & Engineering Solutions of Sandia, LLC, a wholly owned subsidiary of Honeywell International Inc., for the U.S. Department of Energy’s National Nuclear Security Administration under contract DE-NA0003525. This paper

describes objective technical results and analysis. Any subjective views or opinions that might be expressed in the paper do not necessarily represent the views of the U.S. Department of Energy or the United States Government.

Author contributions

I.C., C.P., and A.H. designed the devices. T.V. conducted the optical simulations. M.D. and H.R. did the mechanical simulations. A.J.L. and M.E. supervised the device fabrication. M.Z. designed the PCBs. A.H. built the experimental setup. T.V. and A.H. characterized the devices and analyzed the results. D.E., G.G., and M.E. supervised the project. A.H. and T.V. wrote the manuscript with input from all authors.

Competing interests

D.E. is a scientific advisor to and holds shares in QuEra Computing. Other authors declare no competing interests.

Additional information

Supplementary information The online version contains supplementary material available at <https://doi.org/10.1038/s41467-025-66718-4>.

Correspondence and requests for materials should be addressed to Tom Vanackere, Artur Hermans or Dirk Englund.

Peer review information *Nature Communications* thanks the anonymous reviewers for their contribution to the peer review of this work. A peer review file is available.

Reprints and permissions information is available at <http://www.nature.com/reprints>

Publisher's note Springer Nature remains neutral with regard to jurisdictional claims in published maps and institutional affiliations.

Open Access This article is licensed under a Creative Commons Attribution-NonCommercial-NoDerivatives 4.0 International License, which permits any non-commercial use, sharing, distribution and reproduction in any medium or format, as long as you give appropriate credit to the original author(s) and the source, provide a link to the Creative Commons licence, and indicate if you modified the licensed material. You do not have permission under this licence to share adapted material derived from this article or parts of it. The images or other third party material in this article are included in the article's Creative Commons licence, unless indicated otherwise in a credit line to the material. If material is not included in the article's Creative Commons licence and your intended use is not permitted by statutory regulation or exceeds the permitted use, you will need to obtain permission directly from the copyright holder. To view a copy of this licence, visit <http://creativecommons.org/licenses/by-nc-nd/4.0/>.

© The Author(s) 2025